CONFERENCE PRE-PRINT

PARTICLE TRACING MODELING OF W TRANSPORT UNDER ELECTROMAGNETIC PERTURBATION OF LI PELLET-INDUCED ELMS IN EAST

HUAYI. CHANG, FENG. WANG, MAO. LI
Dalian University of Technology
Dalian, China

JIZHONG. SUN
Dalian University of Technology
Dalian, China
Email: jsun@dlut.edu.cn

Aabstract

A particle-tracing approach is employed to investigate the transport dynamics of W ions affected by electromagnetic perturbation produced by a Li pellet injection induced ELM in EAST. The electromagnetic perturbations from ELMs are obtained from BOUT++ three-field simulations, which are then interpolated onto the grid of particle tracing code as input for full-orbit simulations of W ions. The results reveal that the $\mathbf{E} \times \mathbf{B}$ drift is the primary transport mechanism of W ions during the ELM and that the perturbed electric field is a dominant determining factor. Further study of the effects of pellet deposition location indicates that pellets deposited at the pedestal top are more effective in expelling W ions from the core plasma region and screening W ions from influxing. It is found that the power of W ions expulsion by ELM exhibits a stronger dependence on pellet size when pellets are deposited at the pedestal top, compared with the deposition in the steep-gradient pedestal region. Radial velocity analysis indicates that ELM perturbations tend to increase the average velocity of W ions, with the inward and outward velocity distributions exhibiting approximately symmetric characteristics. It is also observed that W ions have higher radial velocity magnitude as they approach the separatrix, which facilitates the expulsion of them from the boundary region. The density distribution of W impurity aggregation under ITER high-temperature conditions has also been simulated. The results indicate that the pellet which deposited at pedestal top region facilitates the transport of W ions across a wider radial range. Simulations of discharge scenarios with impurity W ions at different initial poloidal locations reveal that those initially deposited on the low-field side are the most prone to the loss of W ions. It also found that W^{30+} ions can be a good representative, instead of multiple charge states of W ions.

1. INTRODUCTION

To enable efficient and sustained plasma discharge, plasma-facing components (PFCs) in tokamak devices must endure extremely high thermal loads. Tungsten has emerged as the candidate material for fusion reactor PFCs due to its exceptional properties [1]. However, the erosion of the PFCs material can lead to the transport of W particles into the core plasma and cause strong radiation, which would cool down the plasma and degrade the plasma performance [2]. Future fusion reactors, including ITER and CFETR [3], are planned to operate in high-confinement mode (H-mode) to optimize high plasma performance. The H-mode is sustainable due to an edge transport barrier (ETB) formed at the plasma edge, which reduces the particle and energy transport significantly across the pedestal plasma. In the ETB region, impurity transport is governed predominantly by neoclassical processes; however, it exhibits a significant Z-dependence wherein the inward convection velocity scales with Z [4]. Periodic giant ELMs transiently release free energy from the ETB region, but also beneficially drive W impurities outward. Therefore, precise and effective control of ELMs are in great demand in the core plasma. Among all methods discovered, the pellet pacing technique tends to maintain small yet high frequency ELMs. This promotes the realization of high-performance operational scenarios featuring small ELMs, such as the grassy ELM regime [5]. Pellet pacing has also showed effectiveness in mitigating W sputtering during ELMs [6]. These properties render it a prospective method for ELM control in ITER [7]. Substantial evidence also indicates that increasing the ELM frequency can expel W impurities [8, 9]. It is essential to investigate the impact of pellet-induced ELMs on W impurity transport. Previous studies [10, 11, 12] have showed that both Li and D_2 pellets can

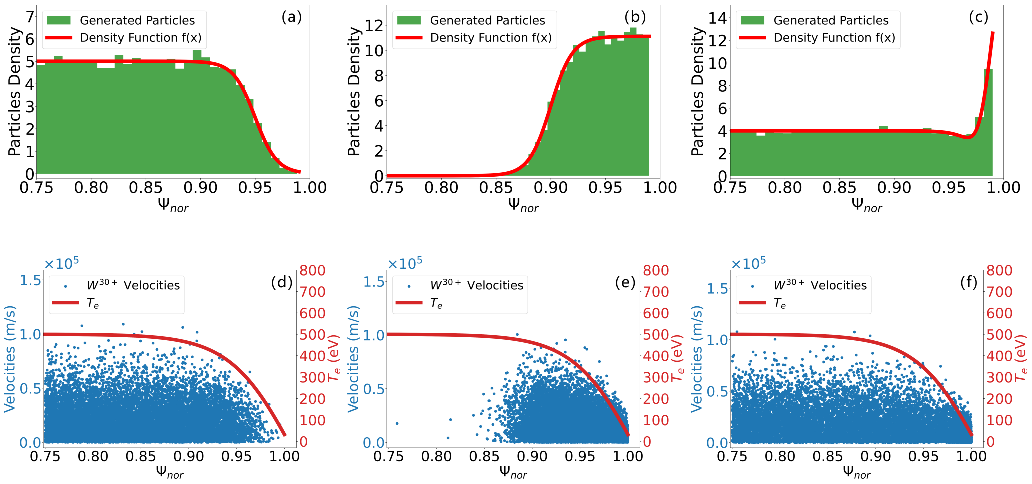

FIG. 1. Three distinct initial density distributions of 12000 W^{30+} ions: (a) W ions distribute near core plasma, (b) W ions gathering around separatrix, and (c) generated from simulation studies on W impurity accumulation in ITER scenarios. The functions $f(x)$ are derived by applying kernel density estimation to the initial W ion density distribution. Their corresponding velocity magnitude distributions and local electron temperature distributions in the respective regions are shown in (d), (e) and (f).

effectively mitigate ELMs. In comparison, Li pellets have some advantages as they do not introduce additional fuel while possess higher ELM triggering efficiency [13].

In the paper, we employ the Particle orbit Tracing Code (PTC) [14] to perform full-orbit simulations of transport of W particles. We focus on the effects of electromagnetic perturbations resulting from ELMs triggered by Li pellets of varying sizes and deposition positions on the transport of W ions. The ELM electromagnetic fluctuation data are obtained from BOUT++ [15] three-field simulations of Li pellet induced ELMs. We have developed a numerical interface that interpolates perturbed electromagnetic fields (electric potential φ and magnetic flux ψ) from BOUT++ simulations onto PTC grids. It enables systematic investigation of charged particle dynamics under turbulent electromagnetic fields.

2. MODEL AND SIMULATION SETUP

The idea of the present work is as follows: first, we use three-field MHD model to obtain the electromagnetic information of ELM. Then, we interpolate the perturbed electric potential and magnetic flux from BOUT++ grid to PTC grid. Finally, we use the interpolated electromagnetic field as input to PTC to simulate the transport of W ions during ELM.

2.1. W transport simulation

The present work employs the particles tracing code (PTC) [14] to fulfill the mission. The electromagnetic fields in PTC are not solved self-consistently; instead, they are provided as input to the code, which can be obtained from experimental measurements or other simulation codes. In this work, the equilibrium electromagnetic fields are derived from EAST shot #70603 at 3.117 s [16], while perturbed fields are obtained from BOUT++ simulations of Li pellet-induced ELMs. Tungsten ions have a relatively small charge-to-mass ratio, their gyro radius in the magnetic field is relatively large, making simulations under the guiding-center approximation potentially inaccurate. Therefore, we opted to use full-orbit simulations in this study.

As shown in Fig. 1 (a), (b) and (c), the initial W ion density distributions are established for a system of 12000 simulated particles, which have a radial coverage ranging from $\Psi_{nor} = 0.75 - 1.00$, a poloidal distribution covering from $\theta = 0 - 2\pi$, and a fixed toroidal distribution at $\phi = 0$. It is noteworthy that in this study, the simulation only tracks W ions located inside the separatrix, while ions outside the separatrix are treated as lost. The firstly two density distributions are selected to study both the ELM-induced expulsion of W ions from the core region and the screening effect against externally introduced W impurities. The third density distribution is derived from two simulation studies on W impurity accumulation in ITER scenarios [17, 18]. Particle velocities are initialized obeying a Maxwell Boltzmann distribution corresponding to local electron temperature. The electron temperature is referenced from EAST experiment [19], the temperature distribution and W particles velocity magnitude distribution are illustrated in Fig. 1 (d), (e) and (f). In the transport simulations of W ions, collisions between particles and the background plasma are neglected, as existing studies [20] have illustrated their limited influence on ELM-driven particle motion. Additionally, regarding the setting of simulation time, the recovery of the pedestal after an ELM burst typically occurs on a timescale of tens of milliseconds [21]. Therefore, the simulation time in this study is limited to a few milliseconds to ensure that the electromagnetic disturbances are induced by a single ELM event.

2.2. Electromagnetic perturbation produced from pellet-induced ELMs

ELM triggering simulations are conducted using the BOUT++ three-field fluid model. The pellet injection simulation covers a radial range of $\Psi_{nor} = 0.85$ to 1.05, where the normalized poloidal magnetic flux Ψ_{nor} is defined as: $\Psi_{nor} = (\Psi - \Psi_{axis})/(\Psi_{separatrix} - \Psi_{axis})$, with Ψ representing the poloidal magnetic flux. ELMs are triggered by the injection of Li pellets, which are simulated using the BOUT++ three-field model [22, 23]. Further details of the BOUT++ two-fluid module are available in references [24, 25, 26]. The effect of pellet is considered as a local perturbation of the plasma pressure [27], which is modeled as a 2D Gaussian function in radial and poloidal directions. It is assumed that the pellet is injected to the mid-plane of the low-field side (LFS) of the plasma. The rate of the modified pressure over the unperturbed one at the most affected position is defined as $R_p = (P_{0,MAP} + P_{1,MAP})/P_{0,MAP}$. Pellets deposit primarily at two locations: the pedestal top (PT) and the steep-gradient pedestal region (SR). The pellet sizes chosen here are $R_p = 1.8$ (PT), $R_p = 2.4$ (PT), $R_p = 2.2$ (SR), and $R_p = 3.6$ (SR).

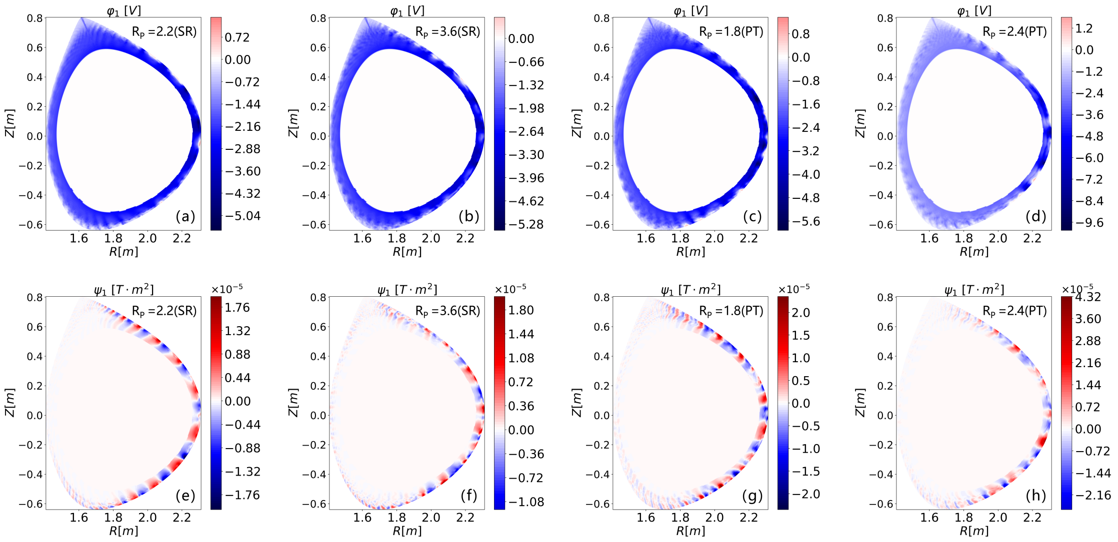

FIG. 2. Perturbed electric potential φ_1 (top row) and perturbed magnetic flux ψ_1 (bottom row) interpolated onto the PTC grid for different pellet deposition scenarios: (a, e) for $R_p = 2.2$ (SR), (b, f) for $R_p = 3.6$ (SR), (c, g) for $R_p = 1.8$ (PT), and (d, h) for $R_p = 2.4$ (PT).

2.3. Interface between BOUT++ and PTC

The mesh generation strategies of the PTC and BOUT++ differ significantly. PTC employs a mesh that is refined in the core and coarser near the boundary, whereas BOUT++ uses a mesh concentrated entirely in the edge region with high resolution. Therefore, for precise field mapping between BOUT++ and PTC computational grids without compromising computational performance, a selective grid refinement approach is implemented exclusively at the PTC boundary regions [28]. An interface is developed to address the interpolation challenges between the two codes. It is capable of reading simulation and mesh data from BOUT++, storing the information, and subsequently interpolating it onto the PTC mesh. Interpolating across distinct grid is achieved using the triangulation method [29]. The perturbed electromagnetic field distributions are obtained from time slices selected after the ELMs burst. Figure. 2 illustrates the interpolated perturbed electric potential φ_1 and perturbed magnetic flux ψ_1 within the PTC grid configuration for the case of $R_p = 2.2$ (SR), $R_p = 3.6$ (SR), $R_p = 1.8$ (PT), and $R_p = 2.4$ (PT). The perturbations caused by different pellets can be reflected by the differences in amplitude magnitudes shown in the figure. The electromagnetic field can be calculated from the following expressions [14, 30]:

$$\boldsymbol{B_{R1}} = \frac{1}{R}\frac{\partial \psi_1}{\partial Z}, \boldsymbol{B_{Z1}} = -\frac{1}{R}\frac{\partial \psi_1}{\partial R}, \boldsymbol{B_{\phi 1}} = -\boldsymbol{\nabla}\psi_1 \times \boldsymbol{B_0} \tag{1}$$

$$\boldsymbol{E_1} = -\boldsymbol{\nabla}\varphi_1 \tag{2}$$

Here, $\boldsymbol{B_{R1}}$, $\boldsymbol{B_{Z1}}$, and $\boldsymbol{B_{\phi 1}}$ represent the radial, vertical, and toroidal components of the magnetic field perturbation, respectively, while $\boldsymbol{E_1}$ denotes the total perturbed electric field.

3. RESULTS AND DISCUSSION

This study begins by comparing the transport of W ions under different electromagnetic field conditions. It then investigates the transport behavior of three distinct W ion density distributions under the influence of electromagnetic fields generated by Li pellets with varying deposition locations and sizes. Subsequently, the evolution of density distributions of W ions with different initial poloidal distributions is examined. Finally, the loss mechanisms of W ions in different valence states under identical ELM conditions are studied.

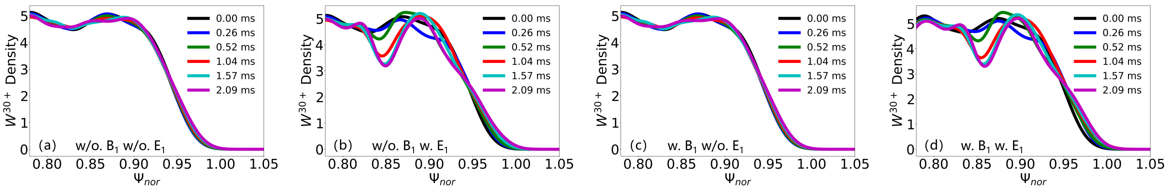

FIG. 3. Temporal evolution of W ions density under different ELM electromagnetic perturbations regime: (a) no perturbed fields, (b) only perturbed electric field, (c) only perturbed magnetic field, and (d) both perturbed electric and magnetic fields. B_1 and E_1 are the perturbed magnetic and electric fields, respectively. The perturbed fields used here are from the case of $R_p = 2.4$ (PT).

3.1. W transport under ELM electromagnetic perturbations

To examine the impact of ELM-induced electromagnetic perturbations on W ion transport, we analyze the temporal evolution of W ion density across varying ELM electromagnetic regimes. All the simulations last $2.06\,\mathrm{ms}$, with initial W ion density distributions correspond to the distribution in Fig. 1 (a). Simulation results of other W ion distributions are qualitatively similar to this pattern, therefore only one set of distribution results is presented in this section. The perturbed electric and magnetic fields employed in this study are characterized from the case $R_p = 2.4$ (PT), which can be calculated from perturbed electric potential ϕ_1 and perturbed magnetic flux ψ_1 (eq. **??**-2, and Fig. 2 (a),(e)). The corresponding results are presented in Fig. 3, where B_1 and E_1 in the figures represent the perturbed magnetic and electric fields, respectively. The results indicate that ELM-driven W transport is predominantly governed by electric field perturbations, with minimal influence from magnetic field perturbations. It also indicates that the radial transport of W ions is primarily driven by the $\mathbf{E} \times \mathbf{B}$ drift. These findings are consistent with the conclusions reported in [20], validating the present model to some degree.

3.2. W ions density evolution under pellet deposition at PT and SR

3.2.1. W ions distribution near core plasma

The initial W ion density distribution adopted in this section corresponds to the distribution shown in Fig. 1 (a). This configuration is utilized to examine the efficacy of ELMs in expelling W ions from the core plasma region. Figure 4 illustrate the evolution of W ion density distributions. Figure 5 illustrates the radial velocity distribution of W ions during ELM perturbations for the case of $R_p = 2.4$ (PT) (Fig. 4 (d)). The radial velocity (v_ψ) distribution across the normalized radial coordinate during ELM perturbations evolves temporally from t = 0 to 5.22 ms. A positive value of v_ψ indicates that the ion velocity is directed outward toward the plasma boundary, while a negative value represents inward velocity toward the plasma core. Blue regions indicate particle probability density at corresponding locations, with color intensity proportional to local probability density at specific velocities. Red lines represent the average magnitude of the velocity of W particles. Green lines display the mean velocity of the W particles, illustrating the degree of asymmetry in their velocity distribution about zero. The blue region gradually expands over time, with both inward and outward transport occurring simultaneously, while the average velocities (green line) show almost no change, consistently remaining near the zero-velocity

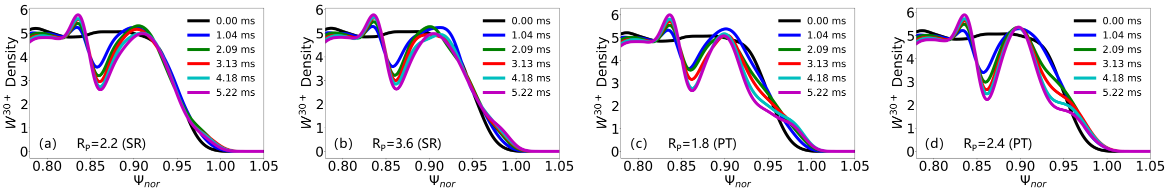

FIG. 4. The temporal evolution of W ion density distributed near the core plasma from 0 to 5.22 ms during ELMs triggered by pellets with different sizes and deposition locations: (a) $R_p = 2.2$ (SR), (b) $R_p = 3.6$ (SR), (c) $R_p = 1.8$ (PT), and (d) $R_p = 2.4$ (PT). The upper row here represents ELMs triggered by pellet injection at the steep-gradient pedestal region, while the lower row shows pellets injected pedestal top.

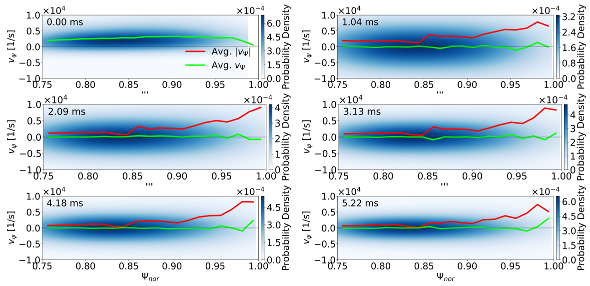

FIG. 5. The radial velocity (v_ψ) distribution across the normalized radial coordinate during ELM perturbations ($R_p = 2.4$ (PT)) evolves temporally from t = 0 to 5.22 ms. Here, a positive value of v_ψ indicates that the ion velocity is directed outward toward the plasma boundary, while a negative value represents inward velocity toward the plasma core. The blue region represents the probability density of particles distributed at that location. The red line represents the average value of the magnitude of the velocity of W particles, while the green line represents the average value of the velocity of W particles.

line. This indicates that ELM has a diffusive effect on the velocity distribution of W ions, with inward and outward transport velocities maintaining a roughly symmetric distribution. Meanwhile, the average magnitude of velocities (red line) exhibit a significant position dependence: the further outward the location, the greater this average value.

Based on the comprehensive results, the impact of ELMs on W impurities near the core region is not simply expulsion or core accumulation, but rather exhibits a more complex behavior. The ELMs reduce W density within a certain radial range while simultaneously increasing it in the adjacent regions. For the PT case, larger pellets induce stronger ELMs that are more effective at expelling W impurities. However, the opposite trend is observed in the SR scenario, likely because the radial region affected by pellet deposition here is narrower, limiting the impact on W impurities distributed near the separatrix. Although larger pellets trigger larger ELMs, they also cause stronger inward transport. The radial influence range of the deposited pellets in the PT region has reached near the boundary. When the velocity distribution is symmetric inward and outward, it will inevitably cause net particle loss, and the larger the ELM size, the more marked the particle loss becomes. The radial velocity magnitude of W ions located near the separatrix is higher, which also facilitates the exclusion of W ions.

3.2.2. W ions distribution around separatrix

To investigate how ELMs triggered by pellets at different locations and sizes affect the shielding of extrinsic W ions, the W ion density distribution shown in Fig. 1 (b) is employed as the initial condition. Figure 6 presents the corresponding results. By observing the density evolution, it is evident that pellet deposition at the pedestal top more effectively shields W ions originating near the separatrix. Moreover, within a certain pellet size range, the shielding capability exhibits a positive correlation with pellet size. However, for pellets deposited in the steep-gradient pedestal region, the shielding effect appears to be largely insensitive to pellet size, and may even exhibit a negative correlation with increasing size. Based on previous studies of pellet-triggered ELMs [23], excessively large pellets may induce ELMs in different radial positions, which could potentially weaken the ELM's transport capability for W particles. Consequently, larger pellets might exhibit inferior transport performance compared to smaller ones. These findings indicate that optimal pellet size selection for ELM triggering is crucial for effective

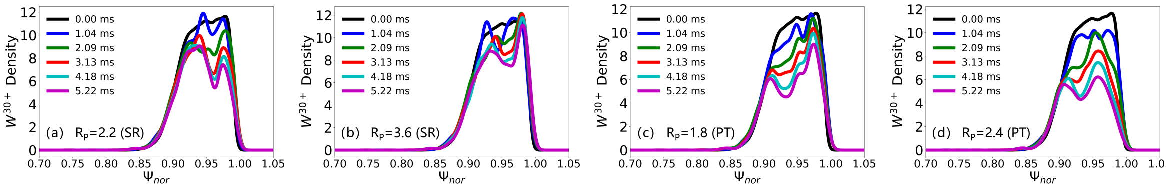

FIG. 6. The temporal evolution of W ion density distributed gather around separatrix from 0 to 5.22 ms during ELMs triggered by pellets with different sizes and deposition locations. The upper row here represents ELMs triggered by pellet injection at the steep-gradient pedestal region, while the lower row shows pellets injected pedestal top.

W impurity removal and screening.

3.2.3. W distribution generated in ITER scenarios

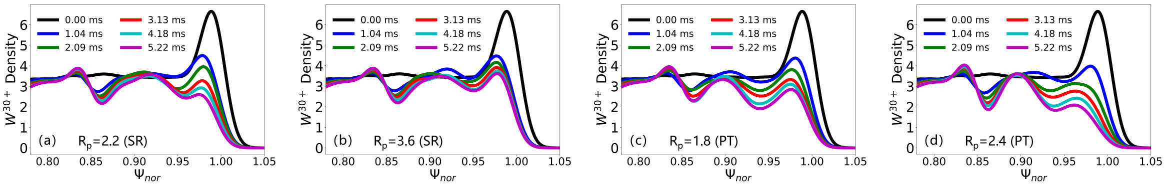

FIG. 7. The temporal evolution of W ion density distributions generated from ITER scenarios from 0 to 5.22 ms during ELMs triggered by pellets with different sizes and deposition locations. The upper row here represents ELMs triggered by pellet injection at the steep-gradient pedestal region, while the lower row shows pellets injected pedestal top.

To investigate the W impurity screening and removal capabilities of pellet-triggered ELMs in future devices like ITER, we conducted additional simulations based on the W impurity distributions taken from modeling [17, 18]. The results are presented in Fig. 7. The evolutions of valid W particles in different cases shows that the particle loss in the case of $R_p = 2.4$ (PT) is the highest among all the cases. These results imply that in future ITER scenarios, ELMs triggered by pellets deposited at the pedestal top are likely to be more effective in expelling W particles from the core region and depleting them out of the separatrix.

3.3. Expulsion W ions initially distributed at different poloidal positions

Given that the above results in the paper are all based on the assumption that W impurities are uniformly distributed across the entire poloidal plane, while the actual situation may not be the case — W impurities are likely to first accumulate in a specific region before spreading across the entire poloidal plane. It is therefore necessary to study radial transport of W ions during this accumulation phase. We distribute W particles beforehand across four distinct poloidal regions (Fig 8 (a)): (1) upper region, (2) high-field side (HFS) region, (3) lower plasma region, and (4) low-field side (LFS) region. The ELM perturbations used here are from the case of $R_p = 2.4$ (PT). Different W ion density poloidal distribution evolution during ELM perturbations from 0 to $5.22\,\mathrm{ms}$ is illustrated in Fig. 8 (b)-(e). From these results, we know that of all four distributions, the mid-plane of the LFS is a good injection location for pellet-induced ELM to remove W particles. Tungsten transport is found to be the least efficient in the HFS region, showing comparably reduced fluxes in both the inward and outward transports. Although the Li pellet deposited at the mid-plane of the LFS of the tokamak is expected to trigger ELMs more efficiently [13], the W ion expulsion is not promising in all poloidal regions. In future devices, it is necessary to consider the exclusion efficiency of W impurity when designing the pellet deposition location.

3.4. Expulsion of W particles with different charge states

The loss characteristics of W particles across various charge states during ELM conditions, specifically for the case of $R_p = 2.4$ (PT), are illustrated in Fig. 9. It should be noted that these results are obtained without rigorous consideration of the relationship between charge states and temperature distributions, representing primarily a verification-oriented simulation outcome. As shown in the figure, the particle loss initially decreases as the charge state increases. In the higher charge state range between 15 and 40, the W particle losses display a complex,

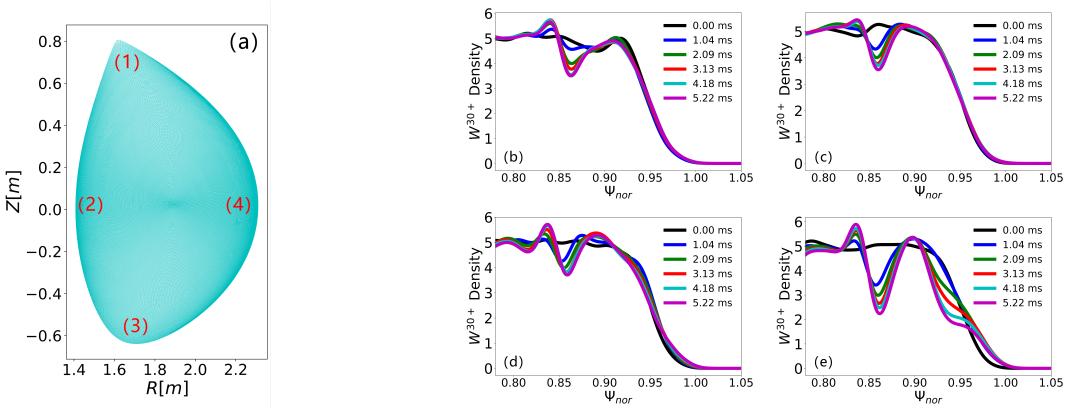

FIG. 8. Initial W ion density distribution at different poloidal positions (a) and the corresponding particle density evolution during ELM perturbations from 0 to $5.22\,\mathrm{ms}$*: (1)-(b), (2)-(c), (3)-(d), and (4)-(e). The ELM perturbations used here are from the case of* $R_p = 2.4$ *(PT). The poloidal positions are defined as follows: (1) divertor region, (2) high-field side (HFS) region, (3) lower plasma region, and (4) low-field side (LFS) region.*

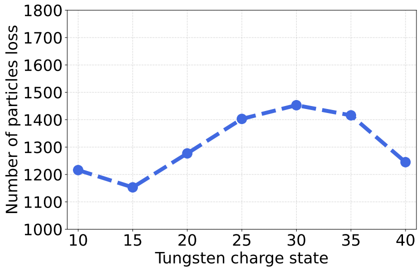

FIG. 9. Particle loss of W ions with different charge states during ELM perturbations. The ELM perturbations used here are from the case of $R_p = 2.4$ *(PT).*

non-monotonic behavior: initially increasing to form a peak at charge state 30, before subsequently decreasing again. W ions losses remain below 1500 particles for all charge states from 10 to 40. Consequently, the selection of W^{30+} as the representative charge state in this study is reasonable for achieving our research objectives. It also indicates that within a certain valence range, the valence state of W ions has no significant influence on its loss variation. Higher valence states are beyond the scope of this study.

4. CONCLUSIONS

In this study, we have developed a simulation framework that integrates BOUT++ and PTC to investigate the transport of W impurities during ELMs triggered by Li pellets. The framework effectively combines the strengths of BOUT++ in simulating ELMs and PTC in modeling W transport, enabling a comprehensive analysis of W impurity behavior under ELM conditions. The W^{30+} ions are selected as the representative charge state for W impurities, and the initial W ion density distribution is established based on kernel density estimation. The results indicate that the electronic field perturbations induced by ELMs play a dominant role in the radial transport of W ions, with minimal influence from magnetic field perturbations. Three different W density distributions are considered in this study to investigate ELM expelling and screening effects on W ions, the third one is based on the W impurity distributions obtained from ITER modeling. ELMs triggered by pellets deposited at the pedestal top exhibit a more pronounced effect compared to those deposited in the steep-gradient pedestal region. The size of the pellet which deposited at the pedestal top also significantly influences the ELM-induced transport of W ions, with larger pellets generally leading to more effective expulsion. Quantitative analysis of the particle loss numbers also verifies the conclusions above. The particles around the separatrix can be easier expelled from the plasma in the case of pellet injection at the pedestal top. The effect of ELMs triggered by pellets on W ions velocity distribution is also analyzed, which reveals that ELMs tend to broaden the velocity distribution range of W impurities. However, no clear tendency of inward or outward transport direction is observed, with the velocity distributions being roughly symmetric between inward and outward directions. It is also found that the closer W ions get to the separatrix, the higher their radial velocity magnitude becomes, ultimately driving their expulsion from the boundary. While the particles in the core region are not significantly expelled, but rather show a tendency to accumulate around the region with the most rapid density depletion. The paper also investigates the impact of ELMs on W ions with different poloidal distributions. The results indicate that W ions in the low-field side (LFS) of the tokamak, where the Li pellet is assumed to be mainly deposited at, exhibit a stronger outward transport tendency compared to other poloidal regions. In the last, the particle loss characteristics of W ions across various charge states are analyzed, it reveals that the peak loss at charge state 30. This proves the feasibility of W^{30+} ions as representative ions in the paper. This further shows that the valence state of W ions exhibits negligible impact on their loss variation across a defined valence range.

ACKNOWLEDGEMENTS

The work is supported by the National Key R&D Program of China under Grant Nos.2019YFE03030004, and the National Natural Science Foundation of China under Grant No.12275040. The authors appreciate the Supercomputing Center of Dalian University of Technology for providing part of the computation resources.

REFERENCES

[1] DAVIS, J. et al., Journal of nuclear materials **258** (1998) 308.

[2] DING, F. et al., Tungsten **1** (2019) 122.

[3] XU, G. et al., Reviews of Modern Plasma Physics **7** (2023) 14.

[4] PÜTTERICH, T. et al., Journal of Nuclear Materials **415** (2011) S334.

[5] XU, G. S. et al., Phys. Rev. Lett. **122** (2019) 255001.

[6] ABRAMS, T. et al., Advances in understanding high-z sourcing, migration, and transport on diii-d from l-mode to highperformance regimes 28th iaea fusion energy conf, 2021.

[7] VIEZZER, E., Nuclear Fusion **58** (2018) 115002.

[8] DUX, R. et al., Nuclear Fusion **51** (2011) 053002.

[9] FEDORCZAK, N. et al., Journal of nuclear materials **463** (2015) 85.

[10] LOARTE, A. et al., Nuclear Fusion **54** (2014) 033007.

[11] SUN, Z. et al., IEEE transactions on plasma science **46** (2017) 1076.

[12] LANG, P. et al., Nuclear Fusion **44** (2004) 665.

[13] LI, M. et al., Nuclear Fusion **64** (2024) 086061.

[14] WANG, F. et al., Chinese Physics Letters **38** (2021) 055201.

[15] DUDSON, B. et al., Computer Physics Communications **180** (2009) 1467.

[16] LUNSFORD, R. et al., Nuclear Fusion **58** (2018) 126021.

[17] FAJARDO, D. et al., Nuclear Fusion **64** (2024) 104001.

[18] LOARTE, A. et al., Evaluation of tungsten transport and concentration control in iter scenarios, in *Preprint: 2016 IAEA Fusion Energy Conf.*, pages PPC–2, 2016.

[19] GAO, X. et al., Physics Letters A **382** (2018) 1242.

[20] VAN VUGT, D. et al., Physics of Plasmas **26** (2019).

[21] BORTOLON, A. et al., Nuclear Fusion **56** (2016) 056008.

[22] XI, P. et al., Nuclear Fusion **53** (2013) 113020.

[23] LI, M. et al., Nuclear Materials and Energy **26** (2021) 100888.

[24] XU, X. et al., Nuclear Fusion **51** (2011) 103040.

[25] XU, X. et al., Communications in Computational Physics, vol. 4, no. 5, July 1, 2008, pp. 949-979 **4** (2008).

[26] XIA, T. et al., Nuclear Fusion **53** (2013) 073009.

[27] GAO, F. et al., Nuclear Fusion **60** (2020) 066022.

[28] ZADORIN, A. I., Computational Mathematics and Mathematical Physics **48** (2008) 1634.

[29] GAO, Z. et al., Computer aided geometric design **29** (2012) 707.

[30] DUDSON, B. et al., Plasma Physics and Controlled Fusion **53** (2011) 054005.